Research in Astron. Astrophys. **2012** Vol. **12** No. **3**, 287–299
http://www.raa-journal.org *http://www.iop.org/journals/raa*

Research in Astronomy and Astrophysics

Interaction and eruption of two filaments observed by *Hinode*, *SOHO*, and *STEREO* *

Ying Li and Ming-De Ding

School of Astronomy and Space Science, Nanjing University, Nanjing 210093, China; Key Laboratory for Modern Astronomy and Astrophysics (Nanjing University), Ministry of Education, Nanjing 210093, China; *dmd@nju.edu.cn*

Received 2011 August 17; accepted 2011 November 17

Abstract We investigate the interaction between two filaments and the subsequent filament eruption event observed from different viewing angles by *Hinode*, the Solar and Heliospheric Observatory, and the Solar Terrestrial Relations Observatory. In the event, the two filaments rose high, interacted with each other, and finally were ejected along two different paths. We measure the bulk-flow velocity using spectroscopic data. We find significant outflows at the speed of a few hundreds of km s^{-1} during the filament eruption, and also some downflows at a few tens of km s^{-1} at the edge of the eruption region in the late stage of the eruption. The erupting material was composed of plasmas with a wide temperature range of 10^4–10^6 K. These results shed light on the filament nature and the coronal dynamics.

Key words: line: profiles — Sun: corona — Sun: filaments — Sun: flares — Sun: UV radiation

1 INTRODUCTION

Solar filaments (prominences) are cold dense plasmas suspended in the corona. Their fine threads are seen in emission as bright prominences at the limb and in absorption as dark filaments against the disk. A filament is formed and maintained above the magnetic polarity inversion line, in a magnetic structure called a filament channel, in which the filament can be supported by the magnetic field. For filament formation and maintenance, Martin (1998) gave a comprehensive review, including the filament structure, chirality, magnetic topology, and mass flows. Filaments would erupt at the onset of MHD instabilities or loss of equilibrium. It is now widely accepted that filament eruption is often associated with other solar activities, such as solar flares and coronal mass ejections (CMEs). Martens & Kuin (1989) considered filaments as the coronal part of an electric current that loses MHD equilibrium at the flare onset and starts to erupt outwards. This leads directly to the observed CME. Kaastra (1985) showed that as the filament moves upwards, a neutral line is formed beneath it, which becomes the site of magnetic reconnection and particle acceleration during the flare. The accelerated particles precipitate into the chromosphere along the field lines, and produce hard X-ray, UV, and optical (such as Hα) emission forming flare ribbons. The energy deposition in the lower atmosphere further causes chromospheric evaporation, which leads to the observed coronal extreme-ultraviolet (EUV) and soft X-ray emissions (Canfield et al. 1982).

* Supported by the National Natural Science Foundation of China.

It has been proposed that two filaments (or filament segments) of the same chirality, when approaching each other, can merge to form long filaments or interact with each other (d'Azambuja & d'Azambuja 1948; Martens & Zwaan 2001). This has been confirmed by observations (Schmieder et al. 2004) and numerical simulations (DeVore et al. 2005; Aulanier et al. 2006). However, in these observations and numerical experiments, the authors found no initiation of an eruption. Theoretically, Martens & Zwaan (2001) presented a "head-to-tail" linkage model for the eruption of filaments. Furthermore, Uralov et al. (2002) suggested that the dual-filament interaction could cause solar eruptions. It is fortunate that there are indeed a few observations indicating that the linkage of two filaments can initiate an eruption. Su et al. (2007) presented new observations of the interaction of two nearby but distinct Hα filaments and their successive eruptions. In the event, the interaction was initiated mainly by an active filament of them. They considered that the second filament eruption may be the result of a loss of stability owing to the sudden mass injection from the first filament eruption. Liu et al. (2010) presented another interesting case: two filaments erupted simultaneously and there was no transfer of material between them during the initial stage; the two filaments merged together along the ejection path, indicating the coalescence between the two interacting flux ropes. Moreover, Bone et al. (2009) reported observations of the interaction and merging of two filaments, one active and one quiescent, and their subsequent eruption. Even so, observations of interacting and erupting filaments are still rare at present.

With the multi-wavelength observations from *Hinode*, the Solar and Heliospheric Observatory (*SOHO*), and the Solar Terrestrial Relations Observatory (*STEREO*), we investigate the interaction and eruption of two filaments. We present observations of the filament interaction and mass ejection, and also measure the bulk-flow velocities of the eruption using spectroscopic data. It is found that the two filaments rise to approach each other, interact, and finally are ejected along two different paths. We describe the observing instruments and data in Section 2. The evolution of the filament interaction and eruption is presented in Section 3. Section 4 gives the bulk-flow velocities of the eruption. Finally, a discussion is given in Section 5.

2 OVERVIEW OF OBSERVATIONS AND INSTRUMENTS

The event of filament eruption was located in the solar active region NOAA 11045. The active region produced several C-class flares and an M-class one within a few hours on 2010 February 8. Among them, a *GOES* C1.8 flare, which started at 11:00 UT and peaked at 11:14 UT, was in close association with the filament eruption. Figure 1 shows the *GOES* 1–8 Å soft X-ray light curve around the flare time. In addition, a white-light CME was first detected with *SOHO*/LASCO at 06:30 UT, having a linear speed of 153 km s^{-1} and lasting about 12 hours.

2.1 Optical Images from *Hinode*/SOT

The filament eruption was observed in Hα images taken with *Hinode*/SOT (Solar Optical Telescope; Tsuneta et al. 2008) with a spatial resolution of $0.16''$ per pixel. SOT observed the event in Hα every half a minute before 10:22 UT and after 12:03 UT, but only obtained one image in between (at 11:41 UT). During this period, SOT was observing the same active region using the Ca II H line with a cadence of ten minutes; thus we can study the evolution of the two flare ribbons. SOT filtergraph magnetograms are not available for this study. Instead, we use the data from *SOHO*/MDI (Michelson Doppler Imager; Scherrer et al. 1995) to study the magnetic field in this active region.

2.2 EUV Images from *SOHO*/EIT and *STEREO*/SECCHI/EUVI

The interaction and eruption of the filaments were observed in EUV by *SOHO*/EIT (Extreme-ultraviolet Imaging Telescope; Delaboudinière et al. 1995) and by the SECCHI/EUVI (Sun Earth Connection Coronal and the Heliospheric Investigation/Extreme UltraViolet Imager; Wuelser et al.

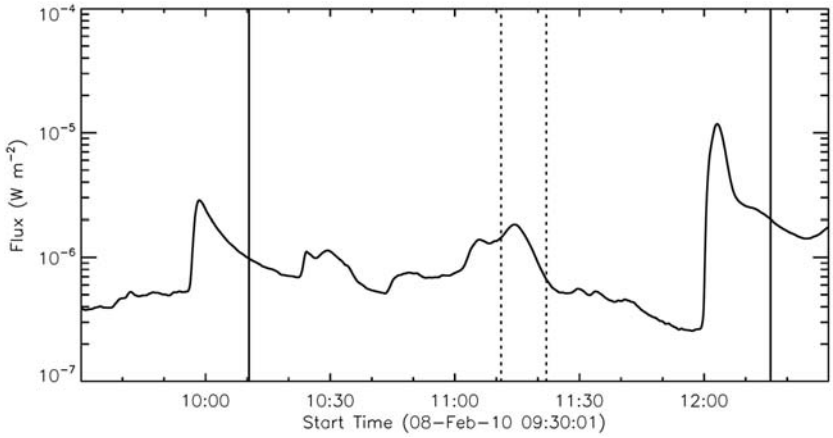

Fig. 1 *GOES* 1–8 Å soft X-ray light curve for a period covering the filament interaction and eruption. The vertical solid lines show the time range of the EIS scan over the active region, while the dotted lines show the time period of the filament eruption.

2004) instrument onboard the *STEREO* spacecraft (A and B). The EIT images were obtained in 195 Å ($\sim 1.5\times10^6$ K) with a cadence of 12 minutes, while the SECCHI/EUVI images were observed in 304 Å ($\sim 6.0\times10^4$ K) and 195 Å with cadences of 10 and 5 minutes, respectively. The active region was located near the center of the solar disk in the EIT field of view (FOV), while it appeared on the east and west limbs in the *STEREO-A* and *B* FOVs, respectively. On that day, these two spacecraft were separated by an angle of $\sim 136^\circ$. We use the EUV data between 10:40 UT and 11:30 UT. This period is from about 20 minutes prior to the flare onset to about 30 minutes after it, thus covering the entire eruption process.

2.3 Spectroscopic Data from *Hinode*/EIS

We measure the Doppler velocities of the mass ejection from spectroscopic data taken with *Hinode*/EIS (Extreme-ultraviolet Imaging Spectrometer; Culhane et al. 2007). EIS covers two wavelength bands, 170–211 Å and 246–292 Å, referred to as the short and long wavelength bands, respectively. These bands include some strong transition region and coronal lines over a wide temperature range. We mainly analyze the Fe XII 195.12 Å line here. In observations, the $2''$ slit of EIS was used to scan the active region of $324''\times376''$ with an exposure time of 45 s. The scanning lasted for 2 hours and 6 minutes, as indicated in Figure 1. Our study focuses on the region hosting the eruption, which has a size of about $30''\times90''$. The EIS slit crossed this region from 11:11 UT to 11:22 UT (between the two vertical dotted lines in Fig. 1). Note that, for all the images from EIS, we use the coordinates in arcseconds relative to a reference point inside the EIS raster FOV.

We reduce the EIS data using the standard processing package. This corrects the detector bias and dark current, as well as hot pixels and cosmic ray hits, resulting in absolute intensities in erg cm^{-2} s^{-1} sr^{-1} Å^{-1}. We also make a correction for a slight tilt of the slit on the CCDs. In addition, we correct for the variation in spectral line positions over the *Hinode* orbit caused by temperature variations in the spectrometer. Such an orbital variation is obtained by averaging the centroid positions over the length of the slit for a quiet region. When measuring the relative Doppler velocity, we use the average line center over a quiet region as the reference Fe XII wavelength.

To interpret the multi-wavelength observations, it is important to co-align the different images. There is an instrumental offset between the images taken in the two EIS CCDs (Young et al. 2007).

To correct this offset, we shift the long wavelength images by 2″ in the solar X-direction and 17″ in the solar Y-direction. To co-align the images from SOT and MDI, we use the sunspots observed by both instruments. The co-alignment between the EIT and EIS data is made using the 195 Å images obtained by both instruments. We estimate the uncertainty of the co-alignment to be within 5″–10″.

3 FILAMENT INTERACTION AND ERUPTION

3.1 The Filaments and Associated Flare

Figure 2 shows the SOT Hα images of the flaring region overlaid with the contours of the MDI magnetogram. The two Hα images were observed ∼40 minutes prior to and after the flare onset at 11:00 UT, respectively. The superimposed MDI magnetogram was taken at 11:15 UT, with contour levels of 200, 500, 900, and 1500 G. There are some strong positive (red contours) and negative (blue contours) magnetic patches. The white arrows (Fig. 2(a)) mark the two filaments prior to the flare onset. Considering the filament morphology and the magnetic configuration, it is reasonable to speculate that the dark segments indicated by the two left arrows are magnetically connected with each other, or that they are the two segments of one large filament. In this context, we only mention one filament, which includes the two segments. After the flare (Fig. 2(b)), the two filaments disappeared, and some post-flare loops (shown by the yellow arrow) appeared instead. From the two Hα images, we find that the filaments erupted between 10:22 UT and 11:41 UT. The interaction between the left and right filaments and their eruption are more clearly presented in the EUV images described in Section 3.2.

Figure 3 shows the evolution of the two flare ribbons. The SOT Ca II H images have the same FOV as the Hα images in Figure 2. The left filament was located between the two flare ribbons, and the right one was on the right side of the ribbons. The two flare ribbons began to brighten at

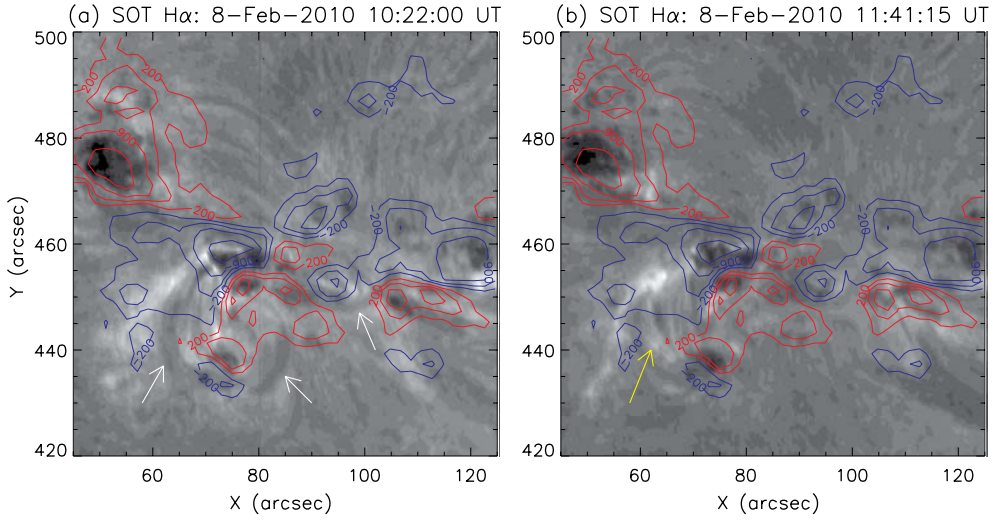

Fig. 2 *Hinode*/SOT Hα images before and after the flare onset at 11:00 UT, superimposed with the MDI magnetogram taken at 11:15 UT on February 8. Red and blue contours refer to the positive and negative polarities, respectively, with levels of 200, 500, 900, and 1500 G. The white arrows in panel (a) point to the two close filaments existing prior to the flare onset. The yellow arrow in panel (b) marks the post-flare loops.

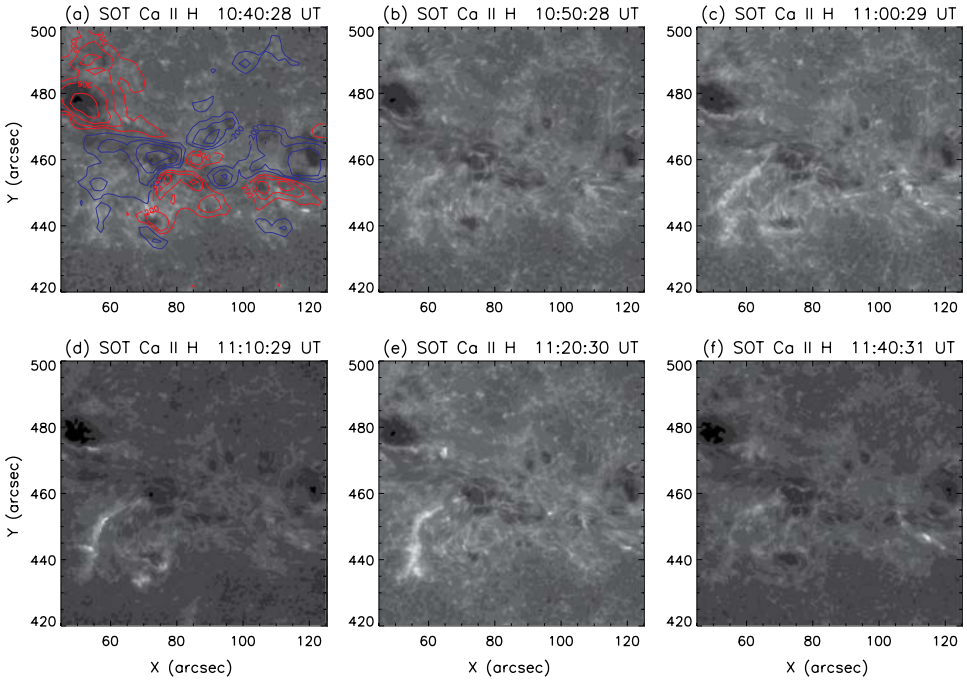

Fig. 3 SOT Ca II H images during the flare. The image in panel (a) is overlaid with the MDI magnetogram taken at 11:15 UT. The MDI contours and the FOV are the same as those in Fig. 2.

∼11:00 UT (Fig. 3(c)). They became the brightest near the peak time of the flare soft X-ray emission (Fig. 3(d)). Tens of minutes later, the ribbons gradually disappeared (Fig. 3(e) and (f)).

3.2 The Filament Interaction and Eruption

The filament interaction and eruption are most evident in EUV images from EIT and SECCHI/EUVI. In the FOVs of these instruments, the eruptions appeared near the center of the solar disk and on the east and west limbs, respectively, as mentioned above. Therefore, we can view this event in three different perspectives. Figures 4 and 5 give the pictures in the filters of 304 Å and 195 Å. Prior to the onset of the flare, we can see the loop expansion due to the filament rising. Some bright loop structures appeared (marked by the black arrows in Figs. 4(a), 4(b), 5(a), 5(c), and 5(e)) at ∼10:56 UT below the core region as compared with the structure at an earlier time (Fig. 5(b)). In particular, there were some loops being contacted (Fig. 5(e)). This may lead to or accelerate the filament interaction and eruption. The two EUV filament channels (EFCs) can be seen in Figures 4(a), 4(b), 5(a), 5(c), and 5(d), as marked by the white arrows. At an early time (∼10:56 UT), both of the filaments were relatively stable. They were rising higher and about to erupt at ∼11:06 UT; meanwhile, the two flare ribbons brightened (see Fig. 3). A few minutes later, the two filaments collided and began to erupt, as shown in Figure 5(i). Due to the low temporal and spatial resolutions, we cannot distinguish which segment (or both segments) of the left filament met the right filament. However, we can judge that the right EFC collided with the left EFC. This was also confirmed by the observation that the ejected material from the filament suddenly changed the direction of ejection: the cool material was expelled to the left side as shown in Figure 5(h) when the two EFCs came into contact with each other (shown

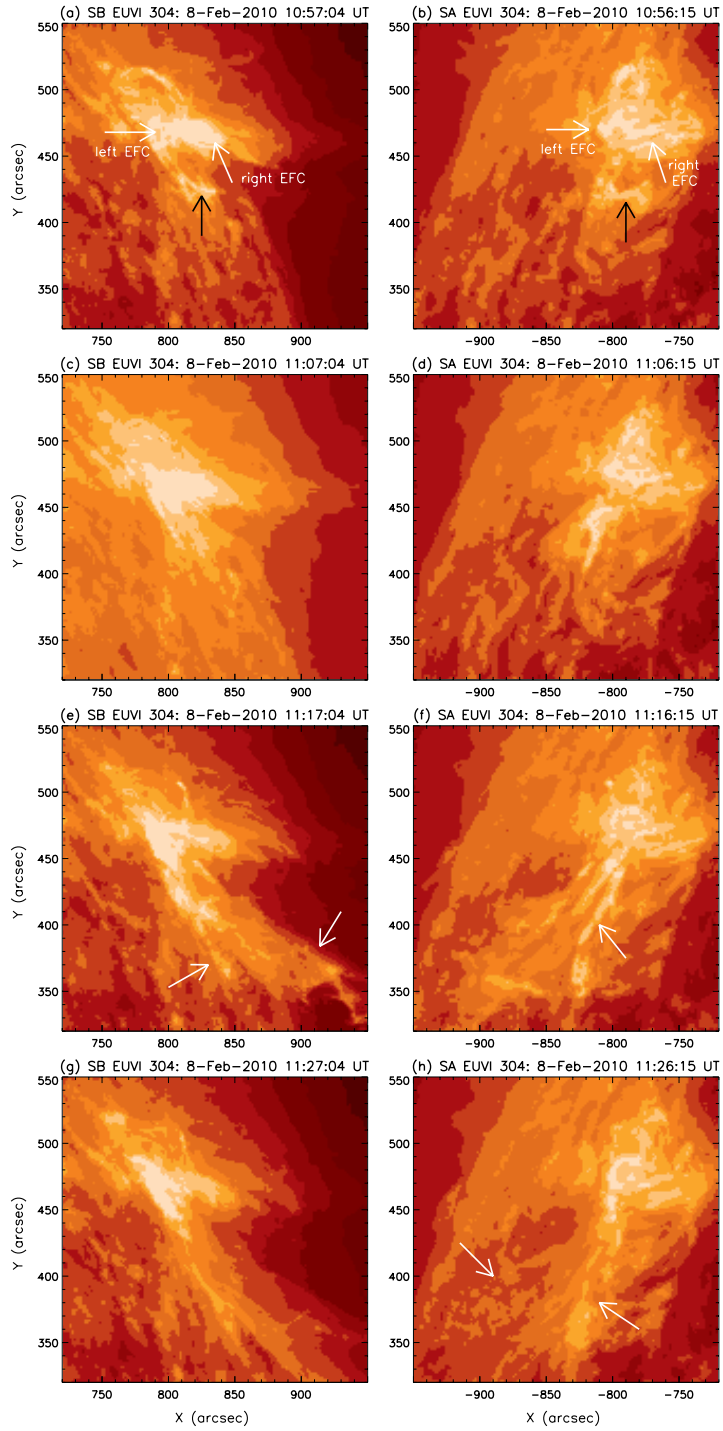

Fig. 4 SECCHI/EUVI 304 Å images of the filament eruption region (evolving from top to bottom). "SA" refers to *STEREO-A* and "SB" to *STEREO-B*. The black arrows in (a) and (b) mark the bright expanding loops. The white arrows point to the filaments or EFCs.

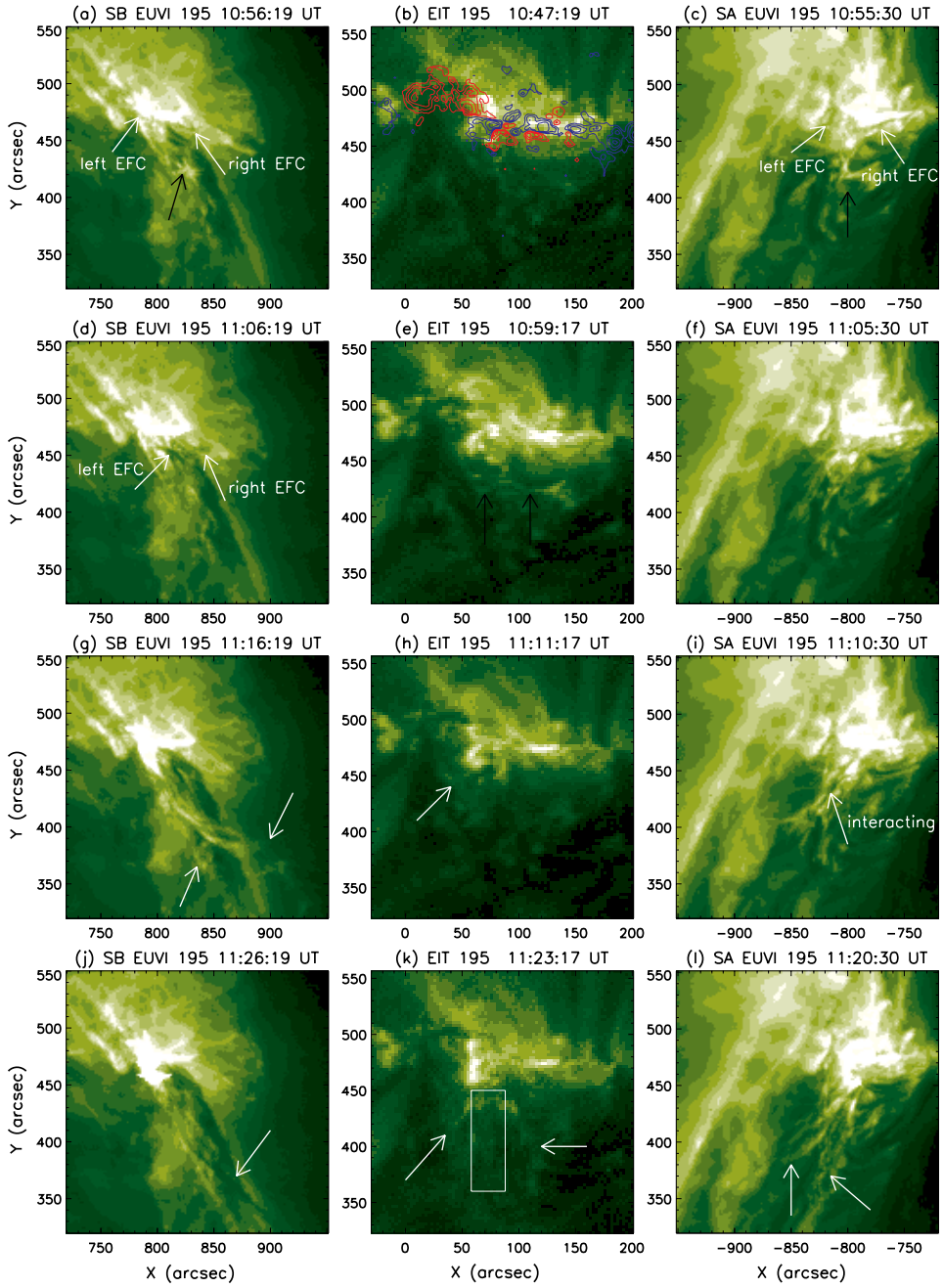

Fig. 5 EIT 195 Å images and EUVI 195 Å images of the filament eruption region (evolving from top to bottom). "SA" and "SB" refer to *STEREO-A* and *STEREO-B*, respectively. In (b), the EIT image is overlaid with the MDI magnetogram taken at 11:15 UT. The black arrows in (a), (c), and (e) mark the bright expanding loops. The white arrows point to the filaments or EFCs. In (k), the white box shows the filament eruption region that we focus on in the study.

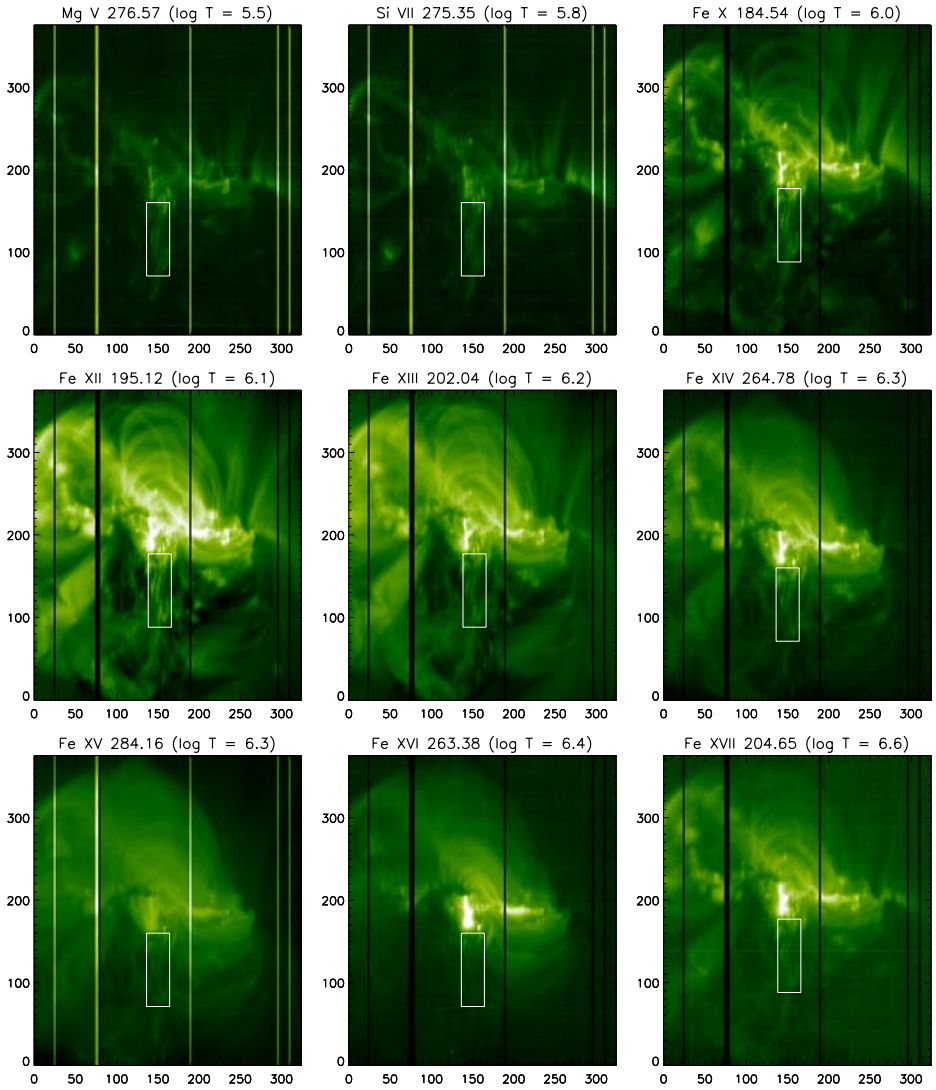

Fig. 6 Intensity maps of the EIS spectral lines. The white boxes mark the main eruption region with the same FOV as the white box in Fig. 5. The filament material is visible in most of these images. Note that the coordinates are relative to a reference point in arcseconds inside the EIS raster FOV (the same for Figs. 7 and 8), and that there is an instrumental offset between the two EIS CCDs recording the short and long wavelength images, respectively. The dark/bright vertical lines refer to missing/abnormal data points.

more clearly in the video 1, available in the electronic edition of the paper). It seems that the two filaments erupted nearly simultaneously after the peak of the flare's soft X-ray emission at 11:14 UT (Figs. 4(e)–(h), 5(g), and 5(l)). Moreover, a careful inspection reveals two ejection paths, marked by the two arrows in Figures 4(e), 4(h), 5(g), and 5(l). Because of the projection effect, the two ejection paths are not clearly visible in EIT images (Fig. 5(k)). The eruptions along different directions can be seen more clearly in the movies (videos 2 and 3). At the later stage of the eruption, some of the

filament material cooled down (Fig. 5(j)) and fell back to the solar surface, while the remainder was ejected into space, as judged from the ejection velocities measured in Section 4.

From different viewing angles (Fig. 5), we see the different manifestations of the filament eruption. Near the solar disk's center, the filament eruption appears rather diffuse; while at the limbs the observed ejection is rather collimated. Furthermore, we observe the different shapes of the erupting filaments from different passbands. In the 304 Å image, the filament ejection is more extended; while in the 195 Å image, the ejected material is more confined. The ejection being visible in emission in a few passbands suggests that the filament material is composed of plasmas with a wide temperature range from 6.0×10^4 K to 1.5×10^6 K (see also Fig. 6). It is possible that part of the filament material is heated to the coronal temperature during the interaction and eruption. An alternative view is that the ejection contains hot plasmas from the reconnection outflow. In a word, cool material ($\sim10^4$ K) and hot material ($\sim10^6$ K) co-exist in the eruption.

4 BULK-FLOW VELOCITIES OF THE ERUPTIONS

The EIS spectroscopic data were obtained by scanning the active region from solar west to east between 10:10 UT and 12:16 UT. Figure 6 shows the intensity maps in EIS spectral lines. The white boxes mark the main eruption region, which was scanned from 11:11 UT to 11:22 UT. During that time, the filaments were erupting. We can see the bright emission from the flare kernel and from the filament eruption in most spectral lines. The filament material is visible in the low temperature line of Mg V ($\sim3.0\times10^5$ K), as well as in the high temperature line of Fe XV ($\sim2.0\times10^6$ K).

Figure 7 shows the Fe XII 195.12 Å intensity and Doppler velocity maps. In this figure, the Doppler velocity is derived from a single Gaussian fitting to the observed spectral line. We detect significant outflows (negative velocities) with a speed of hundreds of km s^{-1} in the eruption region. In addition, the analysis also reveals some weak redshift (positive velocities) of about tens of km s^{-1} near the edge of the region (indicated by the arrows). The redshifts may originate from the cooling

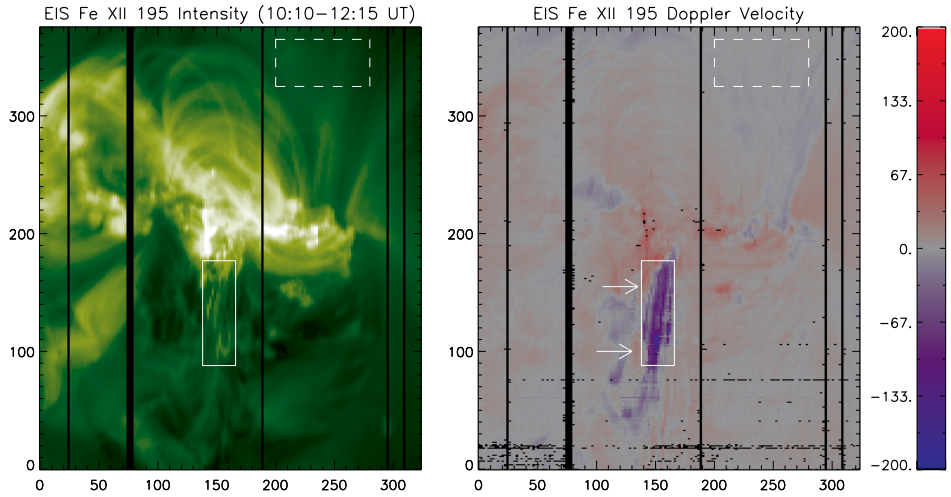

Fig. 7 EIS 195 Å intensity and Doppler velocity maps. The white solid box marks the filament eruption region. The white dashed box represents the quiet region that we use to calculate the reference wavelength. All the values in the velocity panel are obtained from the single Gaussian fitting. The arrows point to the downflow areas at the edge of the main eruption region.

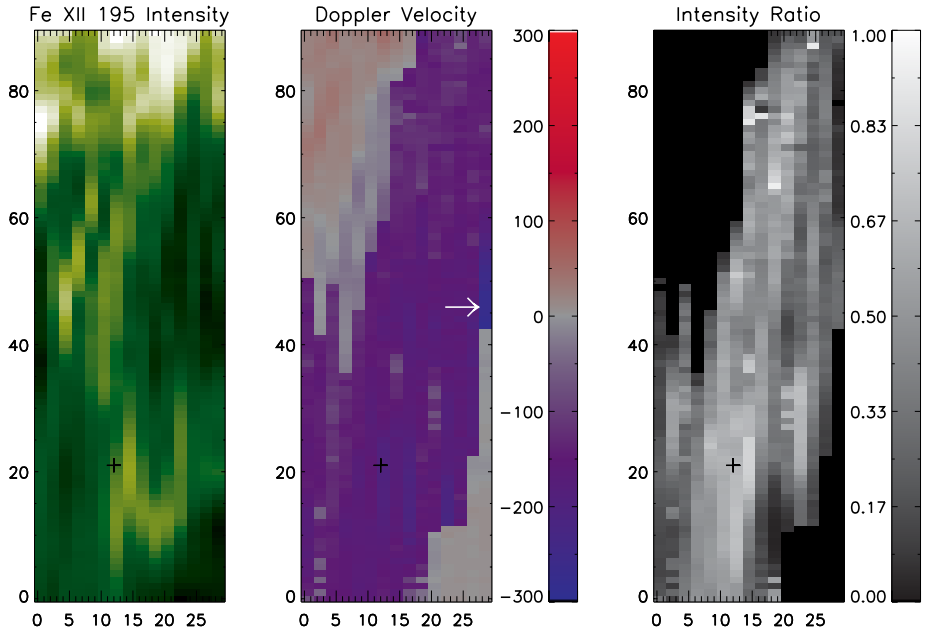

Fig. 8 EIS 195 Å intensity and Doppler velocity maps of the filament eruption region marked by the white solid box in Fig. 7. The velocity field is obtained by combining the results from either the double Gaussian fitting or the single Gaussian fitting. When the double Gaussian fitting is applied, the velocities refer to those of the blueshifted components. The right panel shows the intensity ratio between the blueshifted component and the whole profile. The ratio equals zero when the profile can be well fitted by a single Gaussian function. The white arrow points to the region showing large Doppler velocities over 250 km s^{-1} at the beginning of the eruption. The line profile and its fitting result at the plus sign are shown in Fig. 9.

plasmas, which were falling back to the solar surface at the late stage of the eruption when the EIS slit passed over the edge of the region. When measuring the Doppler velocity, we notice that, in the quiet and redshifted regions, the line profiles can be well fitted by a single Gaussian function; while in the region with significant outflows, the line profiles show obvious double Gaussian components, with a blueshifted component superimposed on a relatively static one. Therefore, we consider using the double Gaussian function to fit the line profiles in the main eruption region.

Figure 8 shows the results of the Fe XII line. In the velocity panel, most of the numbers are derived from a double Gaussian fitting. We also calculate the ratio r of the integrated intensity of the blueshifted component to that of the entire profile. It is plotted in the ratio panel (r becomes zero when the line profile is well fitted by a single Gaussian function). We find that at many locations the blueshifted component is stronger than the static component, i.e., the intensity ratio as defined above is over 0.5.

Figure 9 shows an example of a double Gaussian fitting for the pixel marked by the plus sign in Figure 8. The intensity of the blueshifted component even reaches 67% of the total intensity, and the blueshifted velocity is 195 km s^{-1}. Double Gaussian shapes are also present in other line profiles (such as Fe XIII and Fe XV). In the region marked by the arrow in the velocity panel of Figure 8, the velocity of the blueshifted component can be as high as 300 km s^{-1}, though its intensity is less than half of the total. If corrected for the projection effect, the true velocity may be greater than the escape

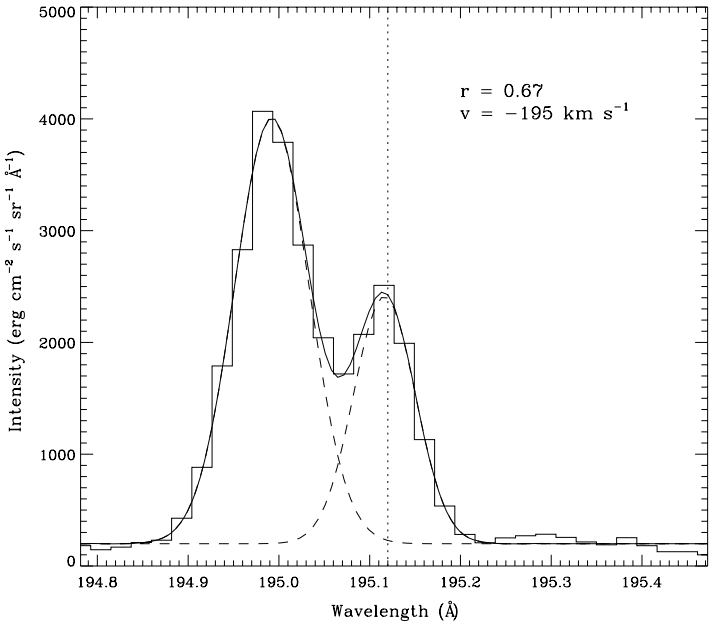

Fig. 9 A typical line profile and its double Gaussian fitting at the plus sign in Fig. 8. The histogram is the observed profile and the solid line is the fitting result. The vertical dotted line refers to the reference wavelength. This line is well fitted by double Gaussian components that are plotted with dashed curves. The velocity for the blueshifted component is 195 km s^{-1}, and its intensity ratio to the whole profile is 0.67.

velocity on the solar surface ($\sim$618 km s^{-1}). It means that there is some material going into space as mentioned in Section 3.2. In fact, the time when the EIS slit scanned this region, $\sim$11:11 UT, corresponds to the onset of the filament eruption.

The spectral line profile in the eruption region cannot be fitted by a single Gaussian function. Although the low spatial resolution of the scanning observation may cause such a deviation from Gaussianity, we think it is more likely that there are multi-velocity components along the line of sight. This is supported by the observation that the two filaments are ejected along different trajectories.

5 DISCUSSION

We study the interaction and eruption of two filaments observed from three different viewing angles. The event was accompanied by a C1.8 two-ribbon flare. At first, we observed the expansion of coronal loops. Then, the two filaments rose higher, interacted with each other, and were finally ejected along two different paths. During the interaction and eruption, the flare ribbons brightened and then gradually decayed. The filament eruption was observed in emission in both the 304 Å image and the 195 Å band, suggesting that the erupted filament material contained plasmas with a wide temperature range of 10^4–10^6 K. We measure the bulk-flow velocities using the EIS spectroscopic data. Significant outflows were detected with a speed of several hundred km s^{-1} during the eruption. Downflows of tens of km s^{-1} were also observed at the edge of the eruption region during the late stage of the eruption. Most of the blueshifted line profiles are double-peaked and can be fitted to two

Gaussians. After correcting for the projection effect, we find that the upward velocity may exceed the solar escape velocity, suggesting that some filament material may have been ejected into space.

This event occurred in an active region that produced a number of large flares. From the movie of the MDI 96-min magnetogram (video 4, available in the electronic edition), we can see that the strong positive and negative magnetic patches were approaching, disintegrating, canceling, and disappearing, especially in the flaring region at $\sim$11:00 UT. From the available data we find that there is a close relationship between the flare and the filament eruption. Before the flare started, the coronal loops appeared to expand. Then the filaments rose higher. Several minutes later, the flare ribbons brightened. It is therefore likely that magnetic reconnection occurred between the two filaments and triggered the filament eruption. As the filaments rose, they began to be linked together, interact with each other, and finally erupted. After the peak of the flare, the filaments were ejected along two different paths. Some of the material escaped from the Sun, and the remainder cooled down and fell back to the solar surface. The interaction of the two filaments may lead to or accelerate the flare energy release.

It has been discussed that pairs of filaments (or filament segments) can merge and interact with each other (d'Azambuja & d'Azambuja 1948; Martin 1998; Martens & Zwaan 2001; Schmieder et al. 2004; DeVore et al. 2005; Aulanier et al. 2006). However, these studies are mainly focused on the filament formation. Observations of the evolution and eruption of filament pairs are valuable and can provide a better understanding of the nature of filaments and coronal dynamics. To our knowledge, Su et al. (2007) reported the first observational study of the interaction between two distinct Hα filaments and the successive eruptions. In their event, the two filaments erupted with an interval of 40 minutes. It was observed that some material was transferred from the filament that erupted first to the other filament, and triggered its eruption. This event was associated with a CME. Quite recently, Liu et al. (2010) presented another interesting event: two filaments erupted simultaneously and there was no mass transfer between them during the initial stage. The two filaments merged together along the ejection path and no CME was observed. Furthermore, Bone et al. (2009) reported observations of the interaction and full merging of the two filaments, one active and the other quiescent, and their subsequent eruption.

In these observational studies, the authors mainly used the ground-based Hα data with high cadence that observes filament plasmas at a low temperature. In our study, however, we use multi-wavelength images in both EUV and Hα to show the interaction and eruption of the two filaments from three different viewing angles. We can compare this event with the previously reported events. The two filaments in this event seem to erupt simultaneously without evident mass transfer between them. This is similar to the case of Liu et al. (2010), but different from the one studied by Su et al. (2007). Moreover, our event was associated with two active filaments, while the event presented by Bone et al. (2009) involved one active filament and one quiescent filament. In particular, we find that the two filaments were ejected along two different paths. These different paths of ejections can be explained by the 3D magnetic reconnection as shown in numerical simulations of Jiang et al. (2011a,b). The magnetic reconnection occurred when the two filaments were rising and interacting with each other. Moreover, in observations, the EFCs did not seem to merge; therefore, they were linked only partially before the filament material was ejected. This may also have some relation to the different ejection paths. The details need to be verified by numerical simulations.

The chirality (handedness) of filaments plays an important role in the merging and linkage of filament pairs. Our results support the scenario that only filaments of the same chirality can link up together (Martens & Zwaan 2001; Schmieder et al. 2004; DeVore et al. 2005; Aulanier et al. 2006; Su et al. 2007). In our event, the two filaments are both dextral, and they link up and interact with each other. This is consistent with previous research.

Spectroscopic data are important for the study of filament heating and coronal dynamics (Li & Ding 2009). In this event, we only analyze the EIS Fe XII 195.12 Å line to obtain the bulk-flow velocity of the filament eruption. In fact, the EIS line profiles are complicated in most regions, especially

in eruption regions. They are often double-peaked, consisting of static and shifted components (Li & Ding 2011), which can be well fitted by double Gaussians. The double-peaked profile may indicate the presence of multiple line-of-sight velocities or may result from the low spatial resolution of the observation. In either case, the dynamics of the filaments and corona are very complicated during the eruption. In addition, we can use the spectroscopic data to measure the temperature and density of filaments and to analyze the plasma heating and cooling during the eruption. To this end, we need spectroscopic data and multi-wavelength images with higher temporal and spatial resolutions.

Acknowledgements The authors would like to thank P. F. Chen, J. Qiu, and Y. Guo for their helpful discussions and the referee for valuable comments on the paper. This work was supported by the National Natural Science Foundation of China (Grant Nos. 10878002 and 10933003) and by the National Basic Research Program of China (973 program, Grant 2011CB811402). *Hinode* is a Japanese mission developed and launched by ISAS/JAXA, collaborating with NAOJ as a domestic partner, and NASA (USA) and STFC (UK) as international partners. Scientific operation of the *Hinode* mission is conducted by the *Hinode* science team organized at ISAS/JAXA. Support for the post-launch operation is provided by JAXA and NAOJ (Japan), STFC (UK), NASA, ESA, and NSC (Norway).

References

Aulanier, G., DeVore, C. R., & Antiochos, S. K. 2006, ApJ, 646, 1349
Bone, L. A., van Driel-Gesztelyi, L., Culhane, J. L., Aulanier, G., & Liewer, P. 2009, Sol. Phys., 259, 31
Canfield, R. C., Gunkler, T. A., Hudson, H. S., et al. 1982, Advances in Space Research, 2, 145
Culhane, J. L., Harra, L. K., James, A. M., et al. 2007, Sol. Phys., 243, 19
d'Azambuja, L., & d'Azambuja, M. 1948, Ann. Obs. Paris Meudon, 6, 7
Delaboudinière, J.-P., Artzner, G. E., Brunaud, J., et al. 1995, Sol. Phys., 162, 291
DeVore, C. R., Antiochos, S. K., & Aulanier, G. 2005, ApJ, 629, 1122
Jiang, R. L., Shibata, K., Isobe, H., & Fang, C. 2011a, ApJ, 726, L16
Jiang, R.-L., Shibata, K., Isobe, H., & Fang, C. 2011b, RAA (Research in Astronomy and Astrophysics), 11, 701
Kaastra, J. S. 1985, Solar flares: An Electrdynamic Model, PhD Thesis, University of Utrecht
Li, Y., & Ding, M.-D. 2009, RAA (Research in Astronomy and Astrophysics), 9, 829
Li, Y., & Ding, M. D. 2011, ApJ, 727, 98
Liu, Y., Su, J., Shen, Y., & Yang, L. 2010, in IAU Symposium 264, eds. A. G. Kosovichev, A. H. Andrei, & J.-P. Roelot, 99
Martens, P. C., & Zwaan, C. 2001, ApJ, 558, 872
Martens, P. C. H., & Kuin, N. P. M. 1989, Sol. Phys., 122, 263
Martin, S. F. 1998, Sol. Phys., 182, 107
Scherrer, P. H., Bogart, R. S., Bush, R. I., et al. 1995, Sol. Phys., 162, 129
Schmieder, B., Mein, N., Deng, Y., et al. 2004, Sol. Phys., 223, 119
Su, J., Liu, Y., Kurokawa, H., et al. 2007, Sol. Phys., 242, 53
Tsuneta, S., Ichimoto, K., Katsukawa, Y., et al. 2008, Sol. Phys., 249, 167
Uralov, A. M., Lesovoi, S. V., Zandanov, V. G., & Grechnev, V. V. 2002, Sol. Phys., 208, 69
Wuelser, J.-P., Lemen, J. R., Tarbell, T. D., et al. 2004, in Society of Photo-Optical Instrumentation Engineers (SPIE) Conference Series 5171, eds. S. Fineschi, & M. A. Gummin, 111
Young, P. R., Del Zanna, G., Mason, H. E., et al. 2007, PASJ, 59, 727